Chapter 5

Spectra and polarization from realistic models of AGN accretion disks, including relativistic effects

5.1 Polarized transfer function

To calculate correctly the flux and polarization coming from an accretion disk around a black hole, especially a Kerr black hole, one must take into account relativistic effects. These include the Doppler shifting and focusing due to the large velocities of the accreting gas around the black hole, gravitational redshifting, and the bending of geodesics as light propagates to the observer at infinity. Cunningham (1975) calculated the flux from an accretion disk around a black hole with arbitrary spin parameter a, normalized to the mass of the black hole. He defined a "transfer function" which is the amplification of the radiation coming from a given radius and redshift when integrating the spectrum of an accretion disk. Speith, Riffert, and Ruder (1995) have done the same calculation, making their code publicly available. Chen and Eardley (1991) have calculated the polarization from rings around Schwarzchild black holes. They derive an algebraic expression for the polarization angle at infinity, using the fact that it is conserved along the photon path due to spherical symmetry of the geometry. Laor, Netzer, and Piran (1990) have calculated the transfer func-

tion using a Monte Carlo code, including polarization based on Connors, Piran, and Stark (1980) and including self-illumination of the accretion disk due to bending of geodesics back towards the disk (Cunningham 1976). They find the polarization at infinity analytically using the Fermi-Walker constant of motion (Chandrasekhar 1983). Bao, Hadrava, and Wiita (1997) have calculated the polarization of "blobs" around a Schwarzchild black hole, using a speedy numerical method to calculate the photon trajectories, and using the same method as Chen and Eardley (1991) to calculate the polarization. There are some disadvantages to each of the above methods of calculating the black hole transfer function: the Laor, Netzer, and Piran method bins all photons into angle bins, so that the positions of different points on the sky are all grouped together; the Speith, Riffert, and Ruder method is rather slow and doesn't include polarization; and the Chen and Eardley and Bao, Hadrava, and Wiita methods are only for Schwarzchild black holes. We are interested in calculating later the effects of microlensing of a quasar, so we need a fast code which can calculate the specific intensity over a grid of points at infinity, to convolve with the amplification pattern of microlensing. Rauch and Blandford (1994) have outlined a method to calculate semi-analytically the geodesics in a Kerr spacetime (see their appendix). We have written a very fast code which integrates the flux and polarization over a grid at infinity, using the expression of the geodesic equations in terms of elliptic integrals and the analytic expression for the parallel propagation of photon polarization from Connors, Piran, and Stark (1980). We have combined this with atmosphere calculations from chapter 3 to calculate the flux and polarization from standard thin accretion disks. This code is also adaptable to other problems such as calculating the line profile and polarization of irradiated disks.

We assume: 1) The disk lies in the equatorial plane, $\mu = 0$, since the height of the disk is much less than the radius of the disk. This is clearly invalid for observers lying close to the plane of the disk, but is probably a good approximation otherwise. Also, when the luminosity approaches Eddington, the disk can become quite thick, which also makes this assumption questionable. 2) The disk is optically thick everywhere so that photons emitted from the disk don't cross the equatorial plane before reaching infinity (if $\mu = 0$ at some point in a photon's trajectory, then it is reabsorbed by the disk; for now we are ignoring such photons, but we plan to eventually take this into account). 3) There are no photons emitted from inside the last marginally stable orbit radius, and photons which cross the equatorial plane inside that last stable circular orbit are

absorbed and not reemitted. 4) The observer is above the disk, so that $\mu > 0$ along the entire geodesic.

In section 5.2, we present the equations for our transfer calculation. Next, we describe the qualitative effects of relativity on the polarization in section 5.3. Then, we present accretion disk models including the effects of relativity in section 5.4. We present our conclusions in section 5.5. Finally, we include an appendix, section 5.6, describing the transfer function calculation in more detail.

5.2 Equations

To compute the transfer function, we choose a grid in impact parameter at infinity (either rectangular or circular) and observed frequency, ν_o, and calculate the total flux and polarized flux (i.e. the Stokes parameters) integrated over the entire disk. We use the impact parameter coordinates α and β (Cunningham and Bardeen 1973) which are defined at infinity as the distances away from the center of the black hole along the axes perpendicular and parallel to the spin axis of the black hole projected on the sky (see figure 5.1. In terms of the momentum of the photon,

$$\alpha = -\lim_{r_o \to \infty} r_o p^{(\phi)}/p^{(t)} \tag{5.1}$$

$$\beta = \lim_{r_o \to \infty} r_o p^{(\theta)}/p^{(t)}, \tag{5.2}$$

where the impact parameters are normalized to r_g. The Stokes parameters integrated over the image of the accretion disk are given by

$$\begin{pmatrix} I \\ Q \\ U \end{pmatrix} = \int I_e(\nu_e, r_e, n_e) g^3 \begin{pmatrix} 1 \\ P_e(\nu_e, r_e, n_e) cos(\psi_o) \\ P_e(\nu_e, r_e, n_e) sin(\psi_o) \end{pmatrix} d\alpha d\beta, \tag{5.3}$$

where ψ_o is the position angle of the polarization as seen by the observer, r_e is the radius at which the photon is emitted (measured in terms of $r_g = GM/c^2$), n_e is the angle with respect to the vertical at which the photon is emitted, I_e and P_e are the intensity and polarization of emitted radiation (from our atmosphere calculations), ν_e is the frequency at which the photon is emitted, and $g = \nu_e/\nu_o$ is the redshift. Thus, we need to calculate r_e, n_e, ν_e, ψ_o as a function of (α, β)

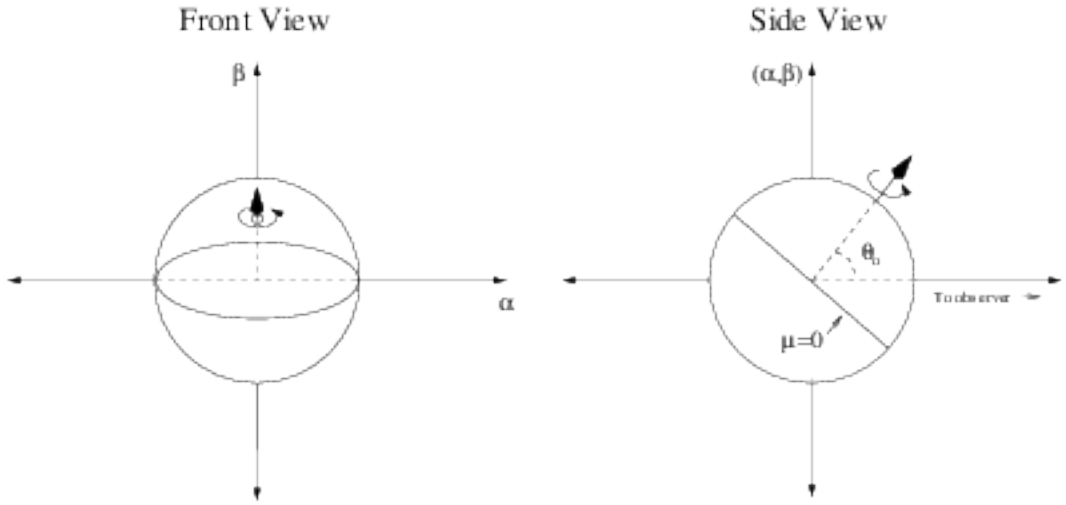

Figure 5.1: Impact parameters at infinity, α and β measured in terms of r_g.

We find r_e first by calculating the radius at which a time-reversed photon with impact parameter (α, β) would cross the equatorial plane.[1] Given the inclination angle of the observer with respect to the disk, $\mu_o = \cos\theta_o$, this determines the constants of motion for photons going towards the observer: $l = L_z/E = -\alpha \sin\theta_o$ and $q^2 = \mathcal{Q}/E = \beta^2 + \mu_o^2(\alpha^2 - a^2)$, where L_z is the z component of the angular momentum, E is the energy at infinity, and $\mathcal{Q}$ is Carter's constant (Carter 1968). We trace the geodesics from infinity, back towards the disk using the equation of motion given by Carter (1968):

$$\int^{r} \frac{dr}{\sqrt{R}} = \pm \int^{\theta} \frac{d\theta}{\sqrt{\Theta}}, \tag{5.4}$$

where R and Θ are functions of r and θ. We rewrite these integrals in terms of $\mu = \cos\theta$ and $u = 1/r$. The integrands change sign whenever a turning point in u or μ is crossed. Thus, to find the radius at which a photon emerged from the disk, one needs to know the number of turning points in μ (i.e. θ) that occur before the photon reaches infinity. If $\beta > 0$ and $\mu > 0$ then the μ starts out increasing. If the photon is to cross the equatorial plane ($\mu = 0$) then it must go through a turning point in μ before μ can start decreasing to zero. If

[1] This is similar to the method used by Perez (1993), Bromley, Chen, and Miller (1997), Dabrowski et al. (1997), and Fanton, Calvani, de Felice, and Čadež (1997).

$\beta \leq 0$, no turning points in μ occur. Once the number of μ turning points are known, one can calculate the integral over μ (or θ) in the equation of motion (5.4). Then , r_e can be calculated using elliptic integrals, as described in detail in the appendix to this chapter. If for a given (α, β) r_e lies inside the innermost stable orbit or outside the outer edge of the range of disk radii, r_{out}, for which atmospheres were calculated, then I_e is set to zero at that point.

Next, we calculate the redshift $g = \nu_e/\nu_o$, which is the ratio of the emitted frequency to the observed:

$$g = -\frac{E}{\mathbf{p_e} \cdot \mathbf{u}} = \frac{e^{\nu}}{\gamma_e(1 - \Omega_e l)}, \tag{5.5}$$

$$e^{\nu} = \sqrt{\frac{\Sigma\Delta}{A}}, \qquad e^{\psi} = \sin\theta\sqrt{\frac{A}{\Sigma}}, \tag{5.6}$$

$$\Sigma = r^2 + a^2\cos^2\theta, \qquad \Delta = r^2 - 2Mr + a^2, \tag{5.7}$$

$$A = (r^2 + a^2)^2 - a^2\Delta\sin^2\theta, \tag{5.8}$$

$$\gamma_e = (1 - v_e^2)^{-1/2}, \qquad v_e = (\Omega_e - \omega)e^{\psi - \nu}, \tag{5.9}$$

$$\Omega_e = \frac{M^{1/2}}{r^{3/2} + aM^{1/2}}, \qquad \omega = \frac{2Mar}{A}, \tag{5.10}$$

$$\tag{5.11}$$

where we have set $G = c = 1$ and the emitting gas is assumed to be on a direct, circular orbit. The angle at which the photon emerges from the plane of the disk is given by

$$\cos n_e = -\frac{\mathbf{p_e} \cdot \mathbf{n}}{\mathbf{p_e} \cdot \mathbf{u}} = \frac{gq}{r_e}, \tag{5.12}$$

where $\mathbf{p_e}$ is the photon 4-momentum at emission, $\mathbf{n}$ is the unit 4-vector normal to the disk (Bardeen, Press, and Teukolsky 1972), and $\mathbf{u}$ is the 4-velocity of accreting gas at r_e, assumed to be in a circular orbit (Cunningham 1975). Then, the polarization and intensity in the emitting frame are calculated by a tri-linear interpolation from atmospheres calculated on a grid of n_e, r_e, and ν_e. For a given n_e, l, and q^2, the photon can emerge in the $+r$ or $-r$ directions (picture a geodesic crossing the equatorial plane at an angle: the photon can either go outwards or inwards depending on which direction it is traveling along the geodesic). The photon is going in the $+r$ direction at infinity, so if there is no turning point along the geodesic, the photon must emerge in the $+r$ direction. If there is a turning point, then the photon must start out in the $-r$ direction. The

polarization vector is then transformed into the locally non-rotating frame, and then parallel-transported to infinity using the Fermi-Walker constant of motion, as described by both Connors et al. (1980) and Chandrasekhar (1983), and summarized in the appendix to this chapter. This gives the polarization angle at infinity, ψ_o, while the degree of polarization $P_e(\nu_e, r_e, n_e)$ remains constant along the geodesic since both Stokes parameters are rotated by the same angle. The intensity at infinity is given by $I_e g^3$ from conservation of photon number, and thus the Stokes parameters are calculated from the intensity and the polarization angle and degree at infinity, and summed over the entire grid to get the total flux and Stokes parameters, as in equation 5.3.

We have compared the part of our code which calculates the final position on a geodesic with the code kindly made available to us by Roland Speith (Speith, Riffert, and Ruder 1995). The results of our code are indistinguishable from those of Speith's code.

5.3 Imaging of an accretion disk

To understand the effects of relativity on the spectrum and polarization of an accretion disk, it helps to visualize the disk. Figure 5.2 shows contours of constant g and constant r_e for a Schwarzchild black hole with a thin disk around it at an inclination of $\mu_o = 0.25$. The disk is rotating counterclockwise, and goes from $6r_g$ to $50r_g$. The photon trajectories are bent towards the observer by the black hole, causing the far side of the disk to appear face-on and thus amplified since it covers more solid angle. The left side is Doppler beamed towards the observer, causing strong blueshift and brightening. Figure 5.3 shows a contour plot of the angle $\cos n_e$ at which the photon emerges from the disk. Since the backside appears closer to face-on, the emerging angle is closer to vertical (i.e. $\cos n_e$ is closer to 1). The blueshifted side is beamed towards the observer, so the emerging angle is closer to vertical. Since the far side and the blueshifted parts appear closer to face-on, their polarizations will be reduced from that of a non-relativistic disk (which would be viewed at a larger inclination angle, or smaller $\cos n_e$).

As the photon propagates to infinity, its polarization is parallel-transported. Since the photons do not come directly to the observer, but are bent by the black-hole gravity, the polarization angle observed from infinity will not be the same as in the rest frame. Assuming that the plane of polarization of the pho-

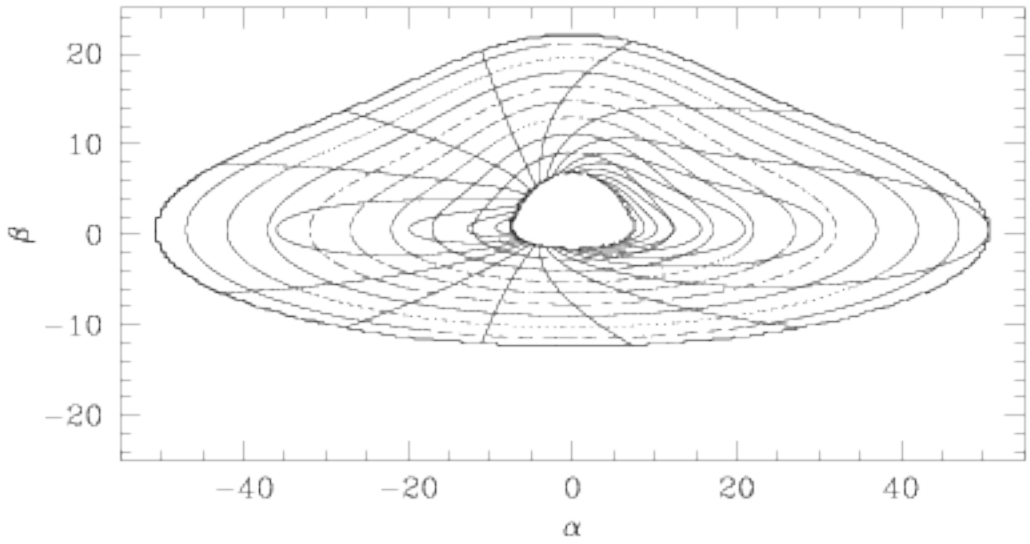

Figure 5.2: Contour plot of the redshift and radius of an accretion disk as seen by an observer at infinity. The radial contours are at $r_e = 6.1, 11, 16, ..., 41, 46, 50$. The redshift contours are $g = 0.55, 0.6, ..., 1.25, 1.3$ (the blue-shifted side is on the left). The inclination of the disk is $\mu_o = \cos(\theta_o) = 0.25$, where $\theta_o = 0$ is for a face-on disk.

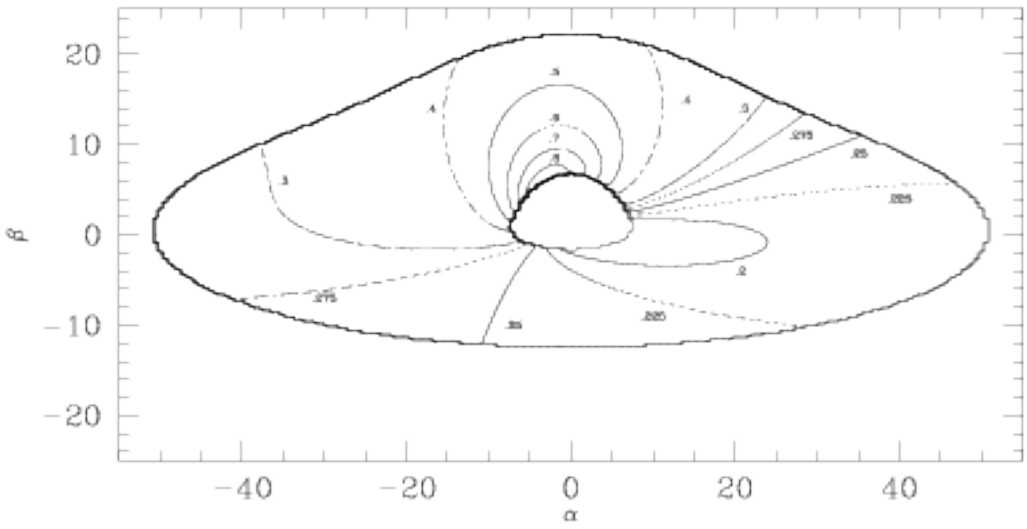

Figure 5.3: Contour plot of $\cos n_e$ (i.e. the cosine of the angle with respect to vertical at which the photon is emitted from the accretion disk). The disk parameters are the same as for the last figure.

ton lies in the plane of the disk in the emitting frame, figure 5.4 shows the polarization angle in the locally non-rotating frame, but plotted as a function of the impact parameter at infinity. The vectors are all the same length, just to illustrate the effects of polarization rotation. Figure 5.5 shows the polarization angle as observed at infinity as a function of impact parameter at infinity. This demonstrates the second depolarizing effect of relativity, since adding polarization vectors at different angles reduces the polarization. Without the effects of relativity, the polarization vectors would all be aligned horizontally.

So, the main two effects of depolarization of an accretion disk by a black hole are: causing the accretion disk to be appear closer to face-on and rotating the plane of polarization.

5.4 Polarization from accretion disks

To check the integration of the polarization over the disk, we have run comparisons with figures 1 and 2 of LNP. Figure 5.6 shows our comparison to figure 1

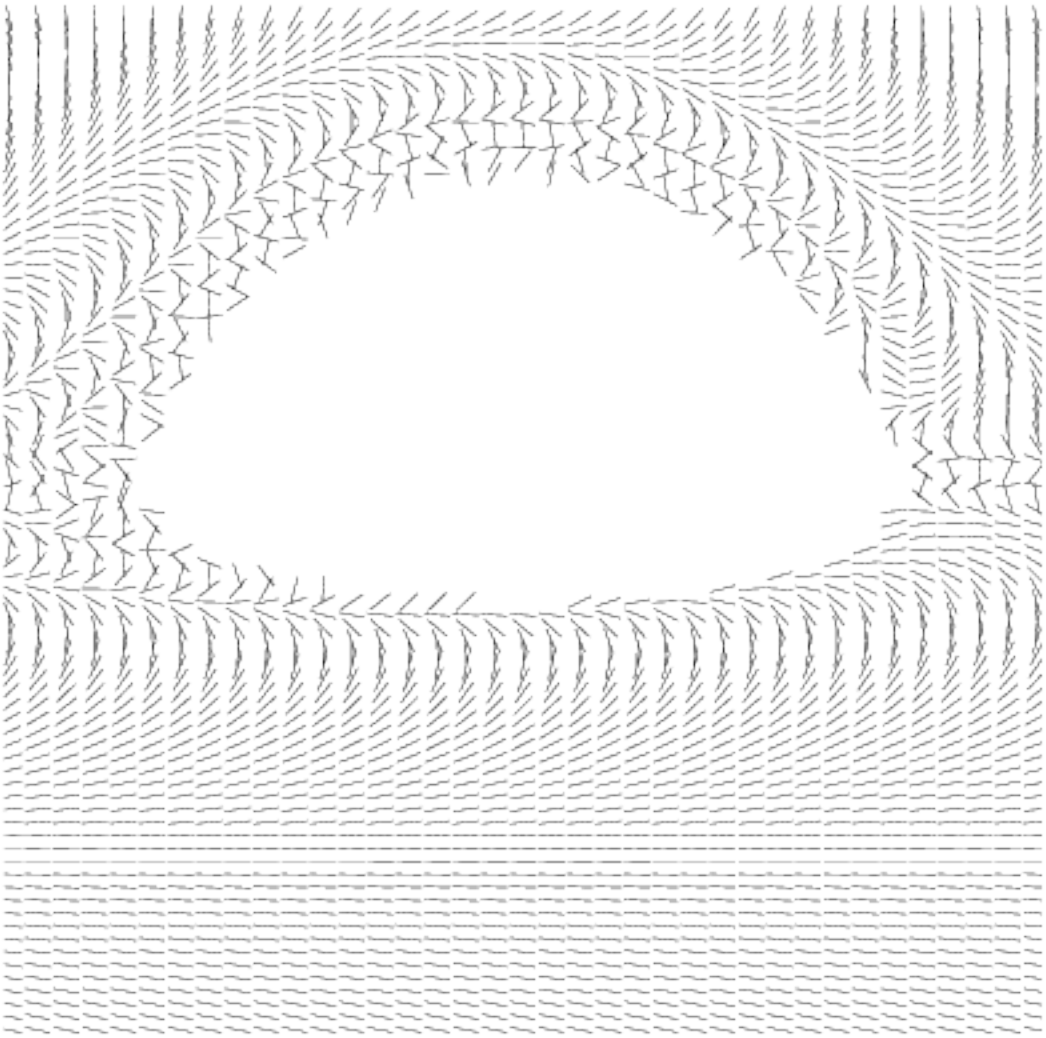

Figure 5.4: Polarization angle in the LNRF, plotted versus the impact parameter at infinity. The horizontal axis is α and the vertical axis is β. Both axes go from -10 to 10.

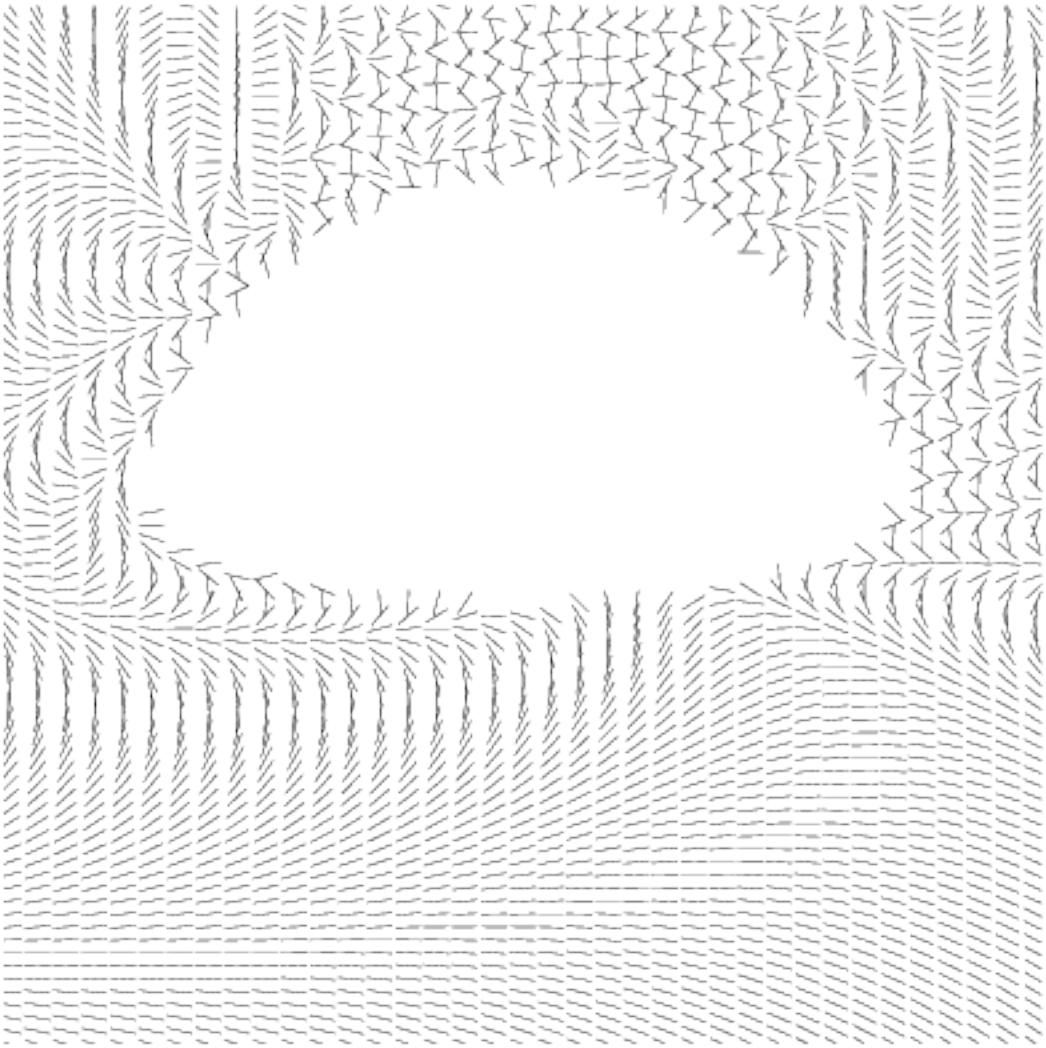

Figure 5.5: Polarization angle as observed at infinity, plotted versus the impact parameter at infinity. The axes are the same as in the previous figure.

of LNP. The agreement looks rather good. Figure 5.7 shows our comparison to figure 2 of LNP. The agreement is not so good for the polarization angle in the $\mu_o = 0.96$ case at high frequencies. However, LNP included self-illumination of the accretion disk, which changes the flux profile in the inner edge of the disk the most, which is where most of the high frequency radiation is emitted and the relativistic effects on the polarization angle are strongest, so the disagreement is not worrisome.

The spectrum and polarization for an entire accretion disk presented in chapter 3 did not include the effects of relativity. Figure 5.8 compares the spectrum and polarization of a disk with and without relativistic effects. The disk calculation assumes a Schwarzchild hole of mass 5.3×10^9 $M_\odot$, $L = 0.092 L_{edd}$, $r_{out} = 50 r_g$. The atmosphere calculations are pure hydrogen with two bound levels explicitly treated. The surface gravity is taken from a one-zone Novikov and Thorne (1973) model, times 1.1 because of the extra opacity. The plot shows the disk viewed at an inclination angle of $\mu_o = 0.27$. The Lyman edge is smeared, but still recognizable, as pointed out by Laor (1992). The total flux is increased and blueshifted due to Doppler beaming, since the disk is viewed close to edge on. Note that the overall polarization is reduced due to the effects discussed above, and the polarization features are blueshifted due to the edge-on inclination. The polarization angle is not changed much by relativistic effects.

The Lyman edge can be severely broadened by relativistic effects. However, if most disks are seen nearly face-on, there will not be as much broadening. It may be possible that non-LTE effects can also cause a reduction in the Lyman edge. We have calculated non-LTE stellar atmospheres for the same disk parameters used in figure 5.8, using the procedures described in chapter 3. The code did not converge for $T_{eff} < 18,500K$, so we used LTE atmospheres for the lower temperature cases. The LTE atmospheres have edges in absorption while the non-LTE atmospheres have edges in emission, which causes some possibly artificial cancellation in the total flux (although the Lyman edge switches from emission to absorption in non-LTE disks calculated by Ivan Hubeny, private communication). Figures 5.9 and 5.10 shows the results of this calculation. Note that the Lyman edge is not very prominent, but there is a change in spectral slope near the edge, and the Balmer edge is almost non-existent. The polarization is qualitatively similar to the full LTE disk.

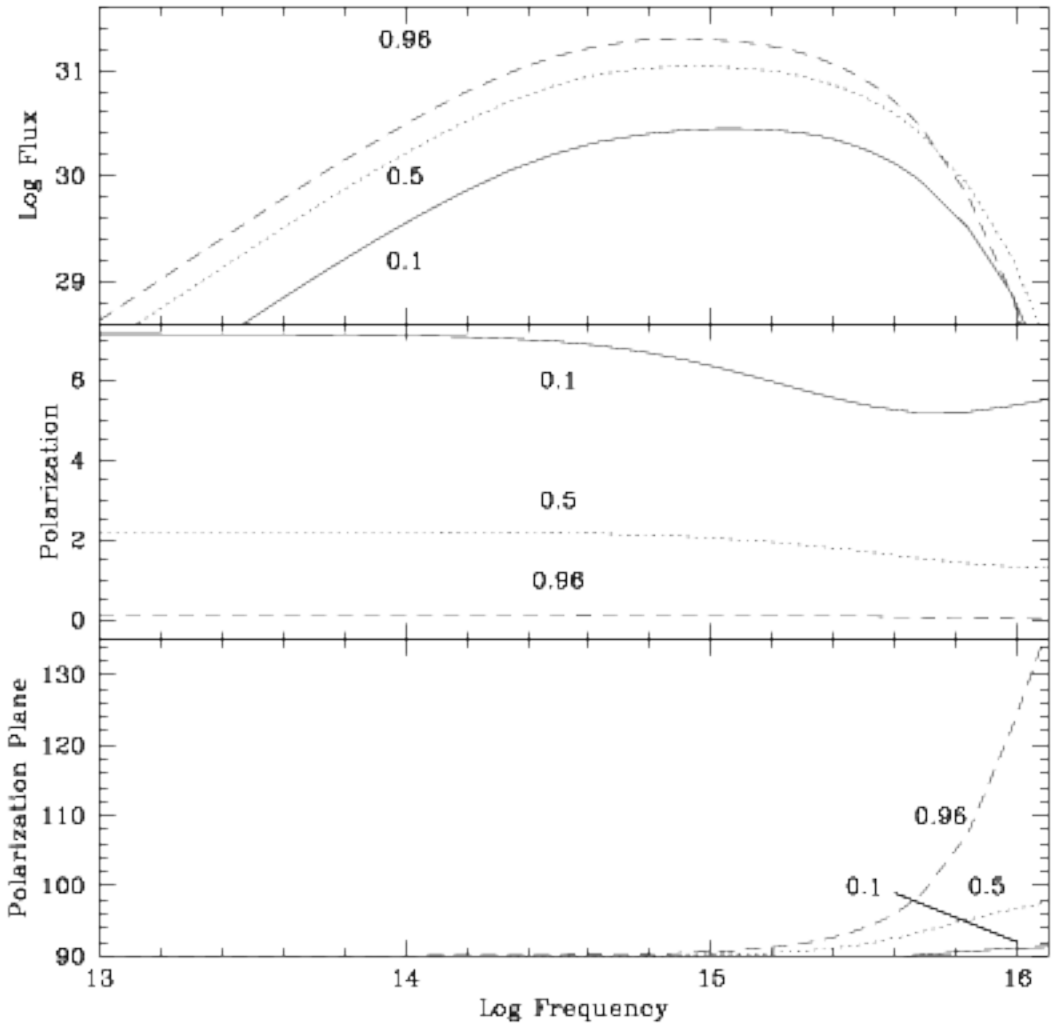

Figure 5.6: Spectrum, polarization, and polarization angle of a blackbody disk around a Schwarzchild black hole with $M = 10^9$ $M_\odot$ and $L = 0.3L_{edd}$, assuming a horizontal disk surface. This figure has the same parameters as LNP figure 1. The results look very similar. The top panel shows the logarithm of the flux in erg $cm^{-2}s^{-1}Hz^{-1}$. The polarization angle is 90° for no rotation.

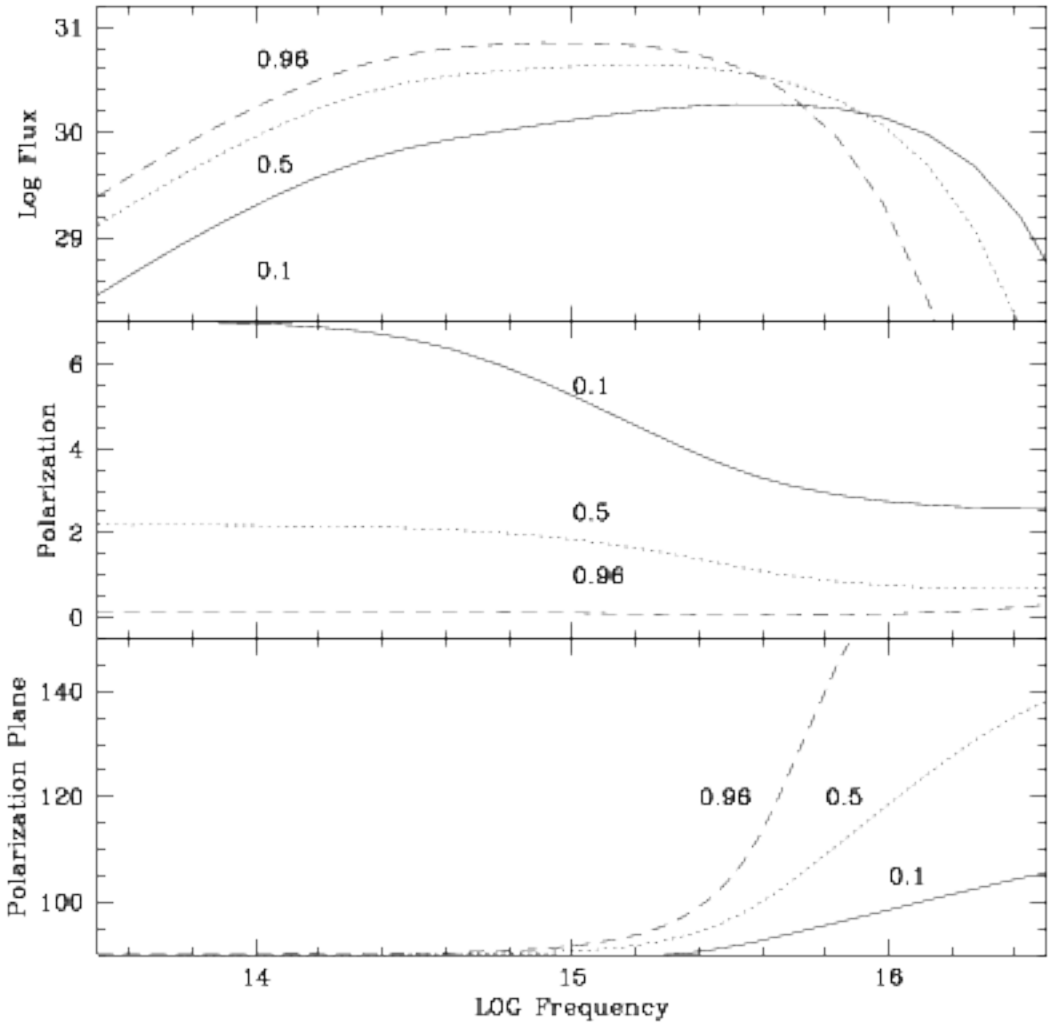

Figure 5.7: Same as figure 5.6, but for a rotating black hole with $a = 0.998$.

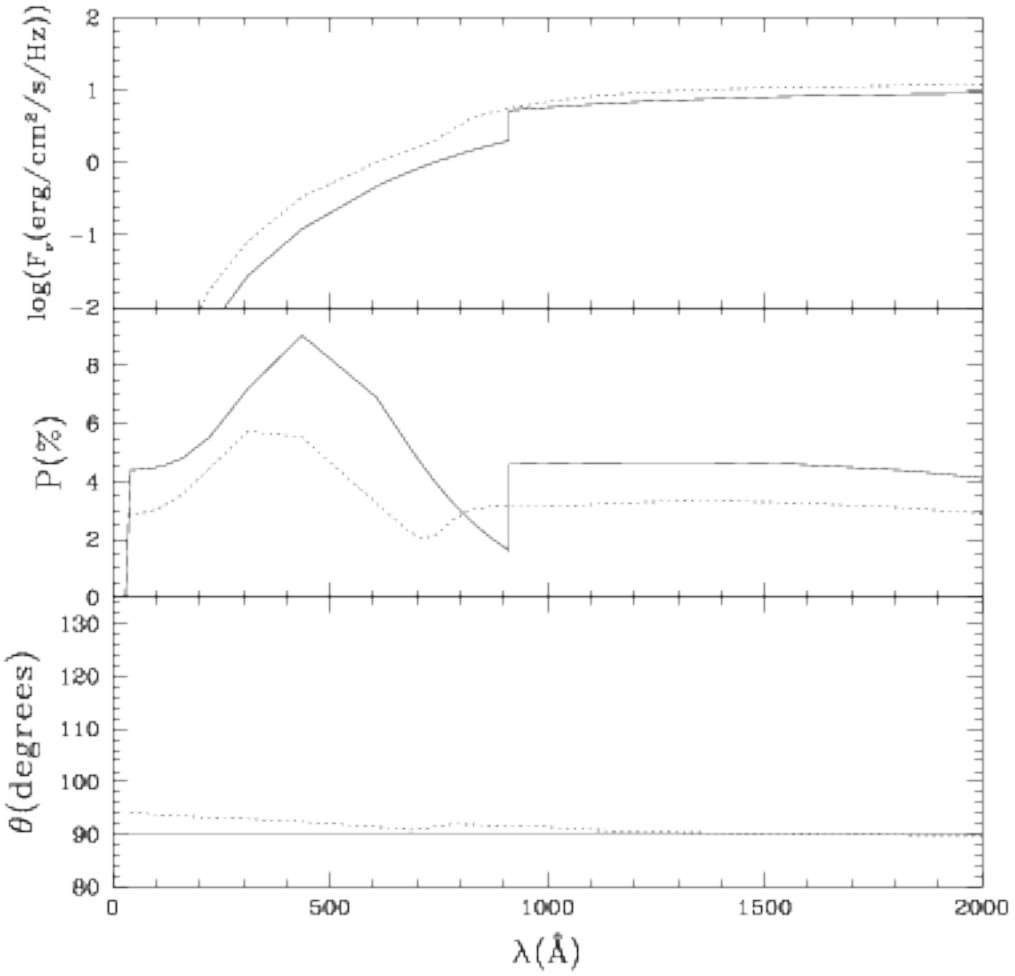

Figure 5.8: Flux, polarization, and polarization angle for a disk with parameters described in the text. The solid curves do not include relativistic effects, which the dashed curves do. The observation angle is $\mu_0 = 0.27$.

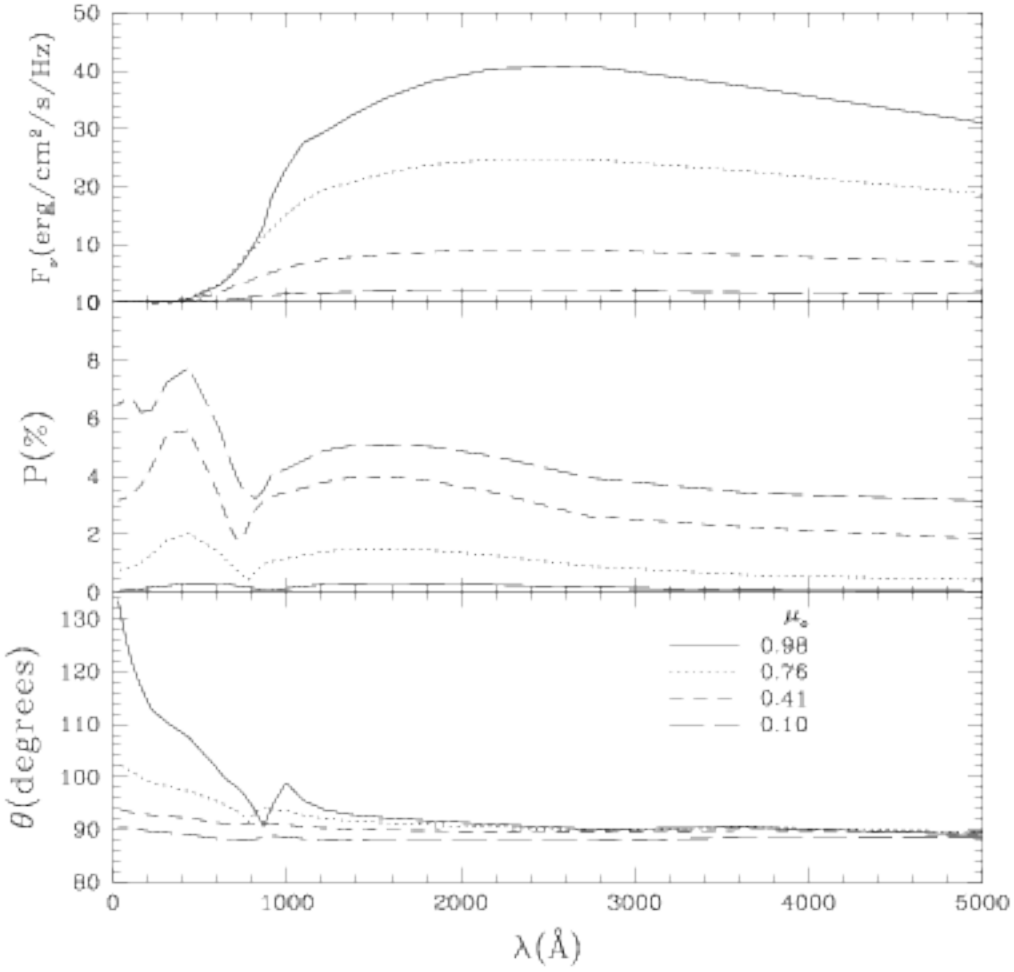

Figure 5.9: Non-LTE disk (for disk annuli with $T_{eff} > 18,500K$).

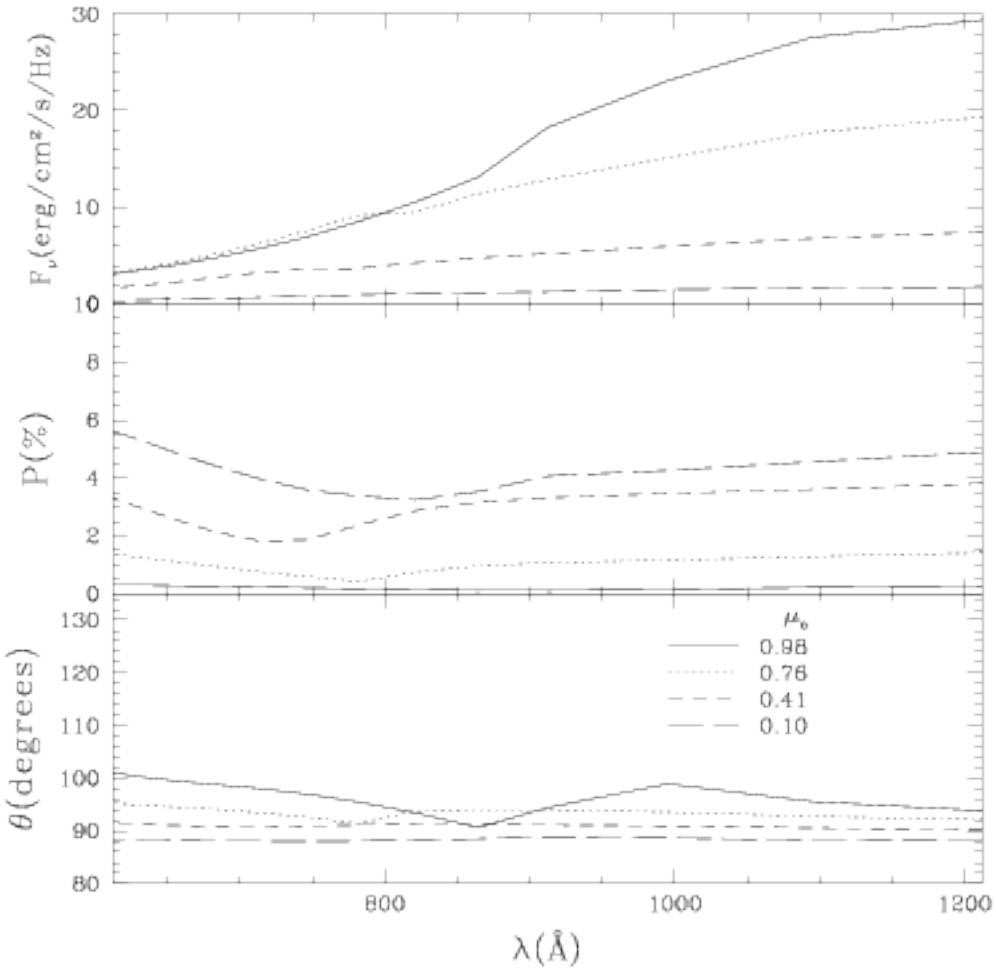

Figure 5.10: Same as figure 5.9, but smaller frequency range near Lyman edge.

5.5 Conclusions

We confirm the findings of LNP that the flux is smeared and polarization is reduced with inclusion of relativistic effects. The polarization rise blueward of the Lyman edge discussed in chapter 3 is reduced and blueshifted when relativistic effects are included. Thus, the polarization rise observed in PG 1222+228 probably does not come from a standard thin accretion disk with pure hydrogen, unless our calculations are strongly modified by including other atomic elements and calculation of the entire vertical structure of the accretion disk.

One possible geometry that might show a rise in polarization is a warped disk which obscures the inner regions which have a strong Lyman emission edge, which is scattered off of the outer parts of the disk. The scattered edge should be strongly polarized and blueshifted due to the Doppler beaming of the inner regions of the disk. Warping can be caused by relativistic precession (Bardeen and Petterson 1975), or radiation instability (Pringle 1996). The Lyman emission edge is rather strong in our non-LTE models, although more sophisticated calculations will be necessary to see how strong this feature is (Hubeny and Hubeny 1997).

5.6 Appendix

5.6.1 Equation of motion

The calculation of geodesics we use follows the approach of Rauch and Blandford (1994). The variables we use are $u = 1/r$ and $\mu = \cos\theta$, where r and θ are the usual Boyer-Lindquist coordinates. Azimuthal symmetry leads to conservation of the angular momentum along the rotational axis of the black hole, L_z. Stationarity leads to conservation of energy (measured at infinity), E. An additional constant of motion was found by Carter (1968): $\mathcal{Q} = p_\theta^2 + \cos^2\theta[L_z^2/\sin^2\theta - a^2E^2]$. When $a = 0$, $\mathcal{Q} + L_z^2 = L^2$, the square of the total angular momentum. Following Rauch and Blandford (1994), we define $l = -p_\phi/p_t = L_z/E$ and $q^2 = \mathcal{Q}/E^2$. The equations of motion of a null geodesic can be written as:

$$H(u_o, u_e) = I(\mu_o, \mu_e). \tag{5.13}$$

The function H is defined as:

$$H(u_o, u_e) = \int_{u_o}^{u_1} \frac{du'}{\sqrt{U(u')}} \mp \int_{u_e}^{u_1} \frac{du'}{\sqrt{U(u')}}, \tag{5.14}$$

where u_o, u_e are the starting and final inverse radii; u_1 is the turning point (if one exists), or some other root of U; and $U(u) = 1 + (a^2 - q^2 - l^2)u^2 + 2[(a - l)^2 + q^2]u^3 - a^2q^2u^4$. The top sign is if there is no turning point in u, the bottom sign is if there is a turning point (this convention will be used throughout this appendix). The roots of U determine the turning points in u: when the photon is unbound, the smallest positive root is the turning point; while if the photon is bound, the second largest positive root is the turning point. When U has four roots, we found them using ZROOTS.F (Press et al. 1992). The function I is defined by:

$$I(\mu_o, \mu_e) = u_{sgn}\mu_{sgn}\left[\int_{\mu_o}^{\mu_+} \frac{d\mu'}{\sqrt{M(\mu')}} \mp \int_{\mu_e}^{\mu_+} \frac{d\mu'}{\sqrt{M(\mu')}}\right] \tag{5.15}$$

where $M(\mu) = q^2 + (a^2 - q^2 - l^2)\mu^2 - a^2\mu^4 \equiv a^2(M_+ - \mu^2)(\mu^2 - M_-)$ and $M_- < M_+$; μ_o, μ_e are the starting and final cosine angles; $\mu_+ = M_+^{-1/2}$ is the turning point (the largest positive root of $M(\mu)$); again, the top sign is for no μ turning point, and the bottom sign is for a μ turning point; and u_{sgn}, μ_{sgn} are the signs of derivatives of r and μ at the starting point (positive for increasing, negative for decreasing). If $q^2 < 0$, then $M_- > 0$, and $M_- \leq \mu^2 \leq M_+$, so the photon never reaches the equatorial plane (however, we include these cases for completeness). If q^2=0, $M_- = 0$, so $0 \leq \mu^2 \leq M_+$. If $q^2 > 0$, $M_- < 0$, and μ has turning points at $\pm\mu_+$.

Our method of calculation is to start at infinity, $u_o = 0$, at a given observation angle, μ_o, and to calculate what the radius of emission, u_e, at the accretion disk where $\mu_e = 0$, given an impact vector (α, β). Thus, we can calculate $I(\mu_o, \mu_e)$ directly, and then solve equation (5.13) for u_e. Equations (5.13-5.15) can be rewritten as:

$$c_1 \int_{u_1}^{u_e} \frac{du'}{\sqrt{U(u')}} = \pm\left[c_1 I(\mu_o, \mu_e) + c_1 \int_{u_1}^{u_o} \frac{du'}{\sqrt{U(u')}}\right] \equiv \pm J, \tag{5.16}$$

where c_1 is defined in table 5.3. The integrals can be expressed in terms of elliptic integrals (or other simpler functions), and inverted in terms of Jacobi functions.

Tables 5.1-5.5 show these functions/inversions for different parameters (these tables are similar to tables 1-6 of Rauch and Blandford 1994, although there are some important changes). When there is a turning point in u, the radius calculation is no different from when there is no turning point. The reason for this can be seen in the following example. When there are four real, distinct roots of U, case 15, the third root, β_3, is the u turning point for unbound photons, so $u \in [0, \beta_3]$. Thus, using Gradshteyn and Ryzhik (1980) or Byrd and Friedman (1971), we can solve equation (5.16) using $u_1 = \beta_3$:

$$\frac{c_1}{\sqrt{a^2 q^2}} \int_{u_e}^{\beta_3} \frac{dt}{\sqrt{(\beta_1 - t)(\beta_2 - t)(\beta_3 - t)(t - \beta_4)}} = F(\tan \phi_f | m_1) = \mp J, \quad (5.17)$$

where $\sin \phi_f = \sqrt{\frac{(\beta_2 - \beta_4)(\beta_3 - u_e)}{(\beta_3 - \beta_4)(\beta_2 - u_e)}}$, and $m_1 = \frac{(\beta_1 - \beta_4)(\beta_2 - \beta_3)}{(\beta_1 - \beta_3)(\beta_2 - \beta_4)}$. Note that we are using the notation of Rauch and Blandford (1994), $F(\tan \phi | m_1)$ instead of the usual $F(\phi | k)$, where $m_1 = 1 - k^2$. This can be inverted as $\sin \phi_f = \pm sn(J|m_1)$, where sn is an elliptic function, and solving for u_e, we get

$$u_e = \frac{(\beta_2 - \beta_4)\beta_3 - (\beta_3 - \beta_4)\beta_2 sn^2 J}{(\beta_2 - \beta_4) - (\beta_3 - \beta_4) sn^2 J}. \quad (5.18)$$

Since the snJ is squared, the dependence on the turning point has vanished. This turns out to be true for all cases where a turning point exists. To find out whether a turning point in u (or r) has occurred, we must simply look at J. Since $\int_{u_e}^{\beta_3} du/\sqrt{U}$ is greater than zero (the integrand is positive definite and $u_e < \beta_3$), then according to equation (5.17), if $J > 0$, then there is a radial turning point, while if $J < 0$, there is not. The above reasoning proceeds similarly for the other cases listed in the tables, and is footnoted in table 5.2. To shorten the presentation in table 5.2, we use the notation $tnJ \equiv snJ/cnJ$ where $snJ \equiv sn(J|m_1)$ and likewise for cn.

Table 5.1: Definition of cases

#	a	q^2	Comment	β_1	β_2	β_3	β_4	u_1[b]	$u \in [,]$
1	0		$q^2+l^2>27$	$(\frac{1}{3},\frac{1}{2})$	$(0,\frac{1}{3})$	<0	...	β_2	$[0,\beta_2]$
2	0		$q^2+l^2>27$	$(\frac{1}{3},\frac{1}{2})$	$(0,\frac{1}{3})$	<0	...	β_1	$[\beta_1,u_+)$
3	0		$q^2+l^2=27$	$\frac{1}{3}$	$\frac{1}{3}$	$-\frac{1}{6}$	...	β_3	$[0,\beta_2)$
4	0		$q^2+l^2=27$	$\frac{1}{3}$	$\frac{1}{3}$	$-\frac{1}{6}$	...	∞	(β_1,u_+)
5	0		$q^2+l^2<27$	$m+in$	$\overline{\beta_1}$	<0	...	β_3	$[0,u_+)$
6	$\neq 0$	0	$l=a$	...	...	...	...	0	$[0,u_+)$
7	$\neq 0$	0	$l=-a$	$m+in$	$\overline{\beta_1}$	$-\frac{a^{-\frac{2}{3}}}{2}$	...	β_3	$[0,u_+)$
8	$\neq 0$	0	$\|l\|\neq a$, 3 real	$>\beta_2$	>0	<0	...	β_2	$[0,\beta_2]$
9	$\neq 0$	0	$\|l\|\neq a$, 3 real	$>\beta_2$	>0	<0	...	β_1	$[\beta_1,u_+)$
10	$\neq 0$	0	$\|l\|\neq a$, 2 equal	$=\beta_2$	$[\frac{1}{4},1]$	<0	...	β_3	$[0,\beta_2)$
11	$\neq 0$	0	$\|l\|\neq a$, 2 equal	$=\beta_2$	$[\frac{1}{4},1]$	<0	...	∞	(β_1,u_+)
12	$\neq 0$	0	$\|l\|\neq a$, 1 real	$m+in$	$\overline{\beta_1}$	<0	...	β_3	$[0,u_+)$
13	$\neq 0$	<0	2 real	$m+in$	$\overline{\beta_1}$	<0	$<\beta_3$	β_3	$[0,u_+)$
14	$\neq 0$	<0	0 real	$m+in$[a]	$\overline{\beta_1}$	$p+ir$[a]	$\overline{\beta_3}$	c_3	$[0,u_+)$
15	$\neq 0$	>0	4 real, distinct	$>\beta_2$	$>\beta_3$	>0	<0	β_3	$[0,\beta_3]$
16	$\neq 0$	>0	4 real, distinct	$>\beta_2$	$>\beta_3$	>0	<0	β_2	$[\beta_2,\beta_1)$
17	$\neq 0$	>0	4 real, 2 equal	$>\beta_2$	$=\beta_3$	$(\frac{1}{4},1)$	<0	β_4	$[0,\beta_3)$
18	$\neq 0$	>0	4 real, 2 equal	$>\beta_2$	$=\beta_3$	$(\frac{1}{4},1)$	<0	β_1	(β_2,β_1)
19	$\neq 0$	>0	2 real	>0	$m+in$	$\overline{\beta_2}$	<0	β_1	$[0,\beta_1]$

[a]Roots are ordered so that $m>p$ and $n>0$.

[b]Cases 1,2,8,9,15,16, and 19 have different u_1 than Rauch and Blandford (1994).

5.6.2 Polarization angle

To find the polarization angle at infinity, we use the method described in (Connors, Piran, and Stark 1980). After calculating the radius of emission, described in the previous subsection, we calculate the contravariant components of the momentum of the photon in the locally non-rotating frame in the equatorial plane, as given in Chandrasekhar (1983), section 63, equation (187)[2]

$$p^t = \frac{1}{r_e^2}\left[\frac{(r_e^2+a^2)\kappa}{\Delta} - a(a-l)\right], \tag{5.19}$$

$$p^r = \pm\frac{1}{r_e^2}\sqrt{\kappa^2 - \Delta\left[(l-a)^2+q^2\right]}, \tag{5.20}$$

$$p^\theta = -\frac{q}{r_e^2}, \tag{5.21}$$

[2]We are using the opposite metric signature of Chandrasekhar (1983): (-,+,+,+).

Table 5.2: Solution for u_e

Case	u_e^c	J	x^d
1[e]	$\frac{\beta_2+m_1\beta_3 sn^2 J}{1+m_1 sn^2 J}$	$Ic_1 - F(x\|m_1)$	$\left[\frac{\beta_2-u_a}{m_1(u_a-\beta_3)}\right]^{1/2}$
2[f]	$\frac{\beta_1-\beta_2 sn^2 J}{cn^2 J}$	$Ic_1 + F(x\|m_1)$	$\left[\frac{u_a-\beta_1}{\beta_1-\beta_2}\right]^{1/2}$
3	$\frac{1}{2}\tanh^2 J - \frac{1}{6}$	$\tanh^{-1} x + \frac{\sqrt{27}}{2} I$	$\left[2u_o + \frac{1}{3}\right]^{1/2}$
4	$\frac{1}{2}\coth^2 J - \frac{1}{6}$	$\tanh^{-1}\frac{1}{x} - \frac{\sqrt{27}}{2} I$	$\left[2u_o + \frac{1}{3}\right]^{1/2}$
5	$c_2 + \beta_3 + \frac{2c_2(1\pm\sqrt{1+tn^2 J})}{tn^2 J}$ [a]	$Ic_1 + F(x\|m_1)$ [a]	$\frac{2[c_2(u_a-\beta_3)]^{1/2}}{\|c_2-u_a+\beta_3\|}$ [b]
6	$u_o - I$	...	...
7	$\frac{\sqrt{3}-1}{c_2} + \frac{2\sqrt{3}(1\pm\sqrt{1+tn^2 J})}{c_2 tn^2 J}$ [a]	$Ic_1 + F(x\|m_1)$ [a]	$\frac{3^{1/4}2(1+c_2u_a)^{1/2}}{\|\sqrt{3}-1-c_2u_a\|}$ [b]
8[e]	$\frac{\beta_2+m_1\beta_3 tn^2 J}{1+m_1 tn^2 J}$	$Ic_1 - F(x\|m_1)$	$\left[\frac{\beta_2-u_a}{m_1(u_a-\beta_3)}\right]^{1/2}$
9[f]	$\frac{\beta_1-\beta_2 sn^2 J}{cn^2 J}$	$Ic_1 + F(x\|m_1)$	$\left[\frac{u_a-\beta_1}{\beta_1-\beta_2}\right]^{1/2}$
10	$\beta_3 + (\beta_2-\beta_3)\tanh^2 J$	$Ic_1 + \tanh^{-1} x$	$\left[\frac{u_a-\beta_3}{\beta_2-\beta_3}\right]^{1/2}$
11	$\beta_3 + (\beta_2-\beta_3)\coth^2 J$	$Ic_1 + \tanh^{-1} x$	$\left[\frac{\beta_2-\beta_3}{u_a-\beta_3}\right]^{1/2}$
12	$c_2 + \frac{2c_2(1\pm\sqrt{1+tn^2 J})}{tn^2 J} + \beta_3$ [a]	$Ic_1 + F(x\|m_1)$ [a]	$\frac{2\sqrt{c_2(u_a-\beta_3)}}{\|c_2-u_a+\beta_3\|}$ [b]
13	$\beta_4 + c_5\frac{\beta_4-\beta_3}{(c_3\pm\sqrt{c_3^2-1})c_4-c_5}$ [a]	$Ic_1 + F(x\|m_1)$ [a]	$\frac{2c_2}{\|1-c_2^2\|}$ [b]
14	$c_3 + \frac{m(1+c_2^2)tnJ}{1-c_2 tnJ}$	$Ic_1 + F(x\|m_1)$	$\frac{u_a-c_3}{m(1+c_2^2)+c_2(u_a-c_3)}$
15[e]	$\frac{\beta_3-c_2\beta_2 sn^2 J}{1-c_2 sn^2 J}$	$Ic_1 - F(x\|m_1)$	$\left[\frac{(\beta_2-\beta_4)(\beta_3-u_a)}{(\beta_2-\beta_3)(u_a-\beta_4)}\right]^{1/2}$
16[f]	$\frac{\beta_3-c_2\beta_2 sn^2 J}{1-c_2 sn^2 J}$	$Ic_1 + F(x\|m_1)$	$\left[\frac{(\beta_1-\beta_3)(u_a-\beta_2)}{(\beta_2-\beta_3)(\beta_1-u_a)}\right]^{1/2}$
17	$\frac{\beta_1\beta_3(1-J)^2-\beta_4\beta_2(1+J)^2+4J\beta_1\beta_4}{\beta_1(1+J)^2-\beta_4(1-J)^2-4J\beta_2}$	$\|c_2 + x\|e^{Jc_1}$	$\frac{2(c_3+\sqrt{c_3(\beta_1-u_a)(u_a-\beta_4)})}{(\beta_1-\beta_4)(\beta_3-u_a)}$
18	$\frac{\beta_1\beta_3(1-J)^2-\beta_4\beta_2(1+J)^2+4J\beta_1\beta_4}{\beta_1(1+J)^2-\beta_4(1-J)^2-4J\beta_2}$	$\|c_2 + x\|e^{Jc_1}$	$\frac{2(c_3+\sqrt{c_3(\beta_1-u_a)(u_a-\beta_4)})}{(\beta_1-\beta_4)(\beta_3-u_a)}$
19[e]	$\beta_1 + \frac{c_4(\beta_4-\beta_1)}{c_4-(-c_3\pm\sqrt{c_3^2-1})c_5}$ [a]	$Ic_1+F(x\|m_1)$ [a] $-2K(m_1)$	$\frac{2c_2}{\|1-c_2^2\|}$ [b]

[a] If $|J| > K(m_1)$, then make $J = 2K(m_1) - |J|$, and the + sign should be chosen in the formula for u_e. Otherwise, leave J as is and choose the $-$ sign in the formula for u_e.
[b] If the quantity in the absolute value sign is < 0, $F(x|m_1)$ becomes $2K(m_1) - F(x|m_1)$.
[d] $x = \tan\phi_o$ for elliptic integral cases. m_1 is defined in table 5.3.
[e] If $J > 0$, then there is a radial turning point.
[f] If $J < 0$, then there is a radial turning point.

Table 5.3: Constants used in table 5.2

Case	c_1^a	c_2	c_3	m_1
1	$\sqrt{\frac{1}{2}(\beta_1-\beta_3)(l^2+q^2)}$	...	...	$\frac{\beta_1-\beta_2}{\beta_1-\beta_3}$
2	$\sqrt{\frac{1}{2}(\beta_1-\beta_3)(l^2+q^2)}$	...	...	$\frac{\beta_1-\beta_2}{\beta_1-\beta_3}$
5	$\sqrt{2c_2(l^2+q^2)}$	$\sqrt{\beta_3(3\beta_3-1)}$	...	$\frac{1}{2}+\frac{6\beta_3-1}{8c_2}$
7	$3^{1/4}c_2$	$2a^{2/3}$	...	$\frac{2-\sqrt{3}}{4}$
8	$\sqrt{\frac{1}{2}(\beta_1-\beta_3)\lvert a-l\rvert}$	...	...	$\frac{\beta_1-\beta_2}{\beta_1-\beta_3}$
9	$\sqrt{\frac{1}{2}(\beta_1-\beta_3)\lvert a-l\rvert}$	...	...	$\frac{\beta_1-\beta_2}{\beta_1-\beta_3}$
10	$\sqrt{\frac{1}{2}(\beta_2-\beta_3)\lvert a-l\rvert}$	...	...	...
11	$-\sqrt{\frac{1}{2}(\beta_2-\beta_3)\lvert a-l\rvert}$	...	...	...
12	$\sqrt{2c_2\lvert a-l\rvert}$	$\sqrt{\beta_3(3\beta_3+c_3)}$	$\frac{a+l}{a-l}$	$\frac{1}{2}+\frac{6\beta_3+c_3}{8c_2}$
13	$\sqrt{-a^2q^2c_4c_5}$	$\sqrt{\frac{c_5(u_a-\beta_3)}{c_4(u_a-\beta_4)}}$	$1+\frac{2}{lm^2J}$	$\frac{(\beta_3-\beta_4)^2-(c_4-c_5)^2}{4c_4c_5}$
14	$\frac{1}{2}(c_4+c_5)\sqrt{-a^2q^2}$	$\sqrt{\frac{4m^2-(c_4-c_5)^2}{(c_4+c_5)^2-4n^2}}$	$m+c_2n$	$\left(\frac{c_4-c_5}{c_4+c_5}\right)^2$
15	$\frac{1}{2}\sqrt{a^2q^2c_3}$	$\frac{\beta_3-\beta_4}{\beta_2-\beta_4}$	$(\beta_1-\beta_3)(\beta_2-\beta_4)$	$\frac{(\beta_1-\beta_4)(\beta_2-\beta_3)}{(\beta_1-\beta_3)(\beta_2-\beta_4)}$
16	$\frac{1}{2}\sqrt{a^2q^2c_3}$	$\frac{\beta_1-\beta_2}{\beta_1-\beta_3}$	$(\beta_1-\beta_3)(\beta_2-\beta_4)$	$\frac{(\beta_1-\beta_2)(\beta_3-\beta_4)}{(\beta_1-\beta_3)(\beta_2-\beta_4)}$
17	$(a^2q^2c_3)^{1/2}$	$\frac{2\beta_3-\beta_1-\beta_4}{\beta_1-\beta_4}$	$(\beta_1-\beta_3)(\beta_3-\beta_4)$	...
18	$-(a^2q^2c_3)^{1/2}$	$\frac{2\beta_3-\beta_1-\beta_4}{\beta_1-\beta_4}$	$(\beta_1-\beta_3)(\beta_3-\beta_4)$	...
19	$(a^2q^2c_4c_5)^{1/2}$	$\sqrt{\frac{c_4(u_a-\beta_4)}{c_5(\beta_1-u_a)}}$	$1+\frac{2}{lm^2J}$	$\frac{(c_4+c_5)^2-(\beta_1-\beta_4)^2}{4c_4c_5}$

[a] This definition is the inverse of that used in Rauch and Blandford (1994).

Table 5.4: Constants used in table 5.2

Case	c_4	c_5
13	$\sqrt{(m-\beta_3)^2+n^2}$	$\sqrt{(m-\beta_4)^2+n^2}$
14	$\sqrt{(m-p)^2+(n+r)^2}$	$\sqrt{(m-p)^2+(n-r)^2}$
19	$\sqrt{(m-\beta_1)^2+n^2}$	$\sqrt{(m-\beta_4)^2+n^2}$

Table 5.5: $I(\mu_o, \mu_e) = u_{sgn}\mu_{sgn}c_I^{-1}[f(\mu_o) \mp f(\mu_e)]$ where the top $-$ sign is when no turning point in μ occurs, and the bottom $+$ sign is when a turning point does occur. s_1 is defined to be the sign of μ_o.

Cases	c_I	$f(\mu)$	μ range	m_1
1-5	$\sqrt{q^2+l^2}$	$\cos^{-1}\left\|\frac{\mu}{\mu_+}\right\|$	$-\mu_+ \le \mu \le \mu_+$	...
6-12	$s_1\sqrt{a^2-l^2}$	$\mathrm{sech}^{-1}\left\|\frac{\mu}{\mu_+}\right\|$	$0 \le s_1\mu \le \mu_+$	...
13-14	$s_1\|a\|\mu_+$	$F\left[\sqrt{\frac{M_+-\mu^2}{\mu^2-M_-}}\middle\| m_1\right]$	$\mu_- \le s_1\mu \le \mu_+$	$\frac{-M_-}{M_+}$
15-19	$s_1\|a\|\sqrt{M_+-M_-}$	$F\left[\sqrt{\frac{\mu_+^2-\mu^2}{\mu^2}}\middle\| m_1\right]$	$-\mu_+ \le \mu \le \mu_+$	$\frac{-M_-}{M_+-M_-}$

$$p^\phi = \frac{1}{r_e^2}\left(-a + l + \frac{a\kappa}{\Delta}\right), \tag{5.22}$$

where $\kappa = r_e^2 + a^2 - al$, Δ is defined in equation (5.5), and the $-$ sign for p^r occurs when there is a turning point in r. From these, we find the photon momentum vector in the tetrad notation:

$$p^{(t)} = r_e\sqrt{\frac{\Delta}{A}}p^t, \tag{5.23}$$

$$p^{(r)} = \frac{r_e}{\sqrt{\Delta}}p^r, \tag{5.24}$$

$$p^{(\theta)} = r_e p^\theta, \tag{5.25}$$

$$p^{(\phi)} = \frac{\sqrt{A}}{r_e}\left(p^\phi - \omega p^t\right), \tag{5.26}$$

where A and ω are defined in equation (5.5). Since the tetrad vector has a Lorentzian metric, we can transform the momentum vector to the emitting frame. We find the parallel polarization vector, which is perpendicular to the momentum vector and lies in the plane of the disk. We then transform the polarization vector to the locally non-rotating frame, and take the component orthogonal to the time component of the momentum vector, $\mathbf{f} = (0, f^i - k^i f^t/k^t)$ which gives the following expression for the contravariant polarization vector:

$$f_{||}^t = 0, \tag{5.27}$$

$$f_{\parallel}^{r} = \frac{\sqrt{\Delta}}{r_e N_f}\left[v_e\left(p^{(t)} - \frac{p^{(r)2}}{p^{(t)}}\right) - p^{(\phi)}\right], \tag{5.28}$$

$$f_{\parallel}^{\theta} = -\frac{v_e p^{(r)} p^{(\theta)}}{p^{(t)} r_e N_f}, \tag{5.29}$$

$$f_{\parallel}^{\phi} = \frac{r_e p^{(r)}}{\sqrt{A} N_f}\left[1 - \frac{v_e p^{(\phi)}}{p^{(t)}}\right], \tag{5.30}$$

where N_f is chosen so that $\mathbf{f}\cdot\mathbf{f} = 1$. We do the same for a polarization vector which is perpendicular to $p_{||}$ and to the photon emission direction:

$$f_{\perp}^{t} = 0, \tag{5.31}$$

$$f_{\perp}^{r} = \frac{\sqrt{\Delta} p^{(\theta)} p^{(r)}}{r_e N_f}\left[-1 + \frac{v_e p^{(\phi)}}{p^{(t)}}\right], \tag{5.32}$$

$$f_{\perp}^{\theta} = \frac{1}{r_e N_f}\left[p^{(r)2} + (1+v_e^2)p^{(\phi)2} - 2v_e p^{(\phi)} p^{(t)} + \frac{v_e p^{(\theta)2} p^{(\phi)}}{p^{(t)}}\right], \tag{5.33}$$

$$f_{\perp}^{\phi} = \frac{r_e p^{(\theta)}}{\sqrt{A} N_f}\left[-(1+v_e^2)p^{(\phi)} + v_e p^{(t)} + \frac{v_e p^{(\phi)2}}{p^{(t)}}\right], \tag{5.34}$$

which is again normalized by N_f. Polarization at an arbitrary angle can be represented by $\mathbf{f} = \cos\psi_e \mathbf{f}_{\parallel} + \sin\psi_e \mathbf{f}_{\perp}$, where $\psi_e = 0$ represents polarization in the plane of the disk. This allows us to calculate the constants of motion which describe the parallel propagation along the photon's trajectory:

$$A_c = p^t f^r + a(p^r f^{\phi} - p^{\phi} f^r), \tag{5.35}$$

$$B_c = (r_e^2 + a^2)(p^{\phi} f^{\theta} - p^{\theta} f^{\phi}) - a p^t f^{\theta}, \tag{5.36}$$

where we have assumed $f^t = 0$ and $\mu_e = 0$ in this equation. This finally allows the computation of the polarization angle at infinity:

$$\psi_o = \tan^{-1}\left[\frac{\beta B_c - \gamma_c A_c}{\beta A_c + \gamma_c B_c}\right], \tag{5.37}$$

$$\gamma_c = -\alpha - a\sqrt{1-\mu_o^2}, \tag{5.38}$$

where $\psi_o = 0$ corresponds to polarization parallel to the α axis. Chandrasekhar (1983) uses a definition for α with the opposite sign used by Cunningham and Bardeen (1973) and us.

We have compared the results of the polarization angle subroutine using Speith's code to calculate the geodesics (since his code integrates over (r_e, g) rather than (α, β)) with the results of other workers. Figure 5.11 shows our plot with the same variables as figure 3 in Chen and Eardley (1991). Figure 5.12 shows our plot with the same variables as figure 3 in Connors, Piran, and Stark (1980). There are no distinguishable differences between the figures produced by our code and those in these papers.

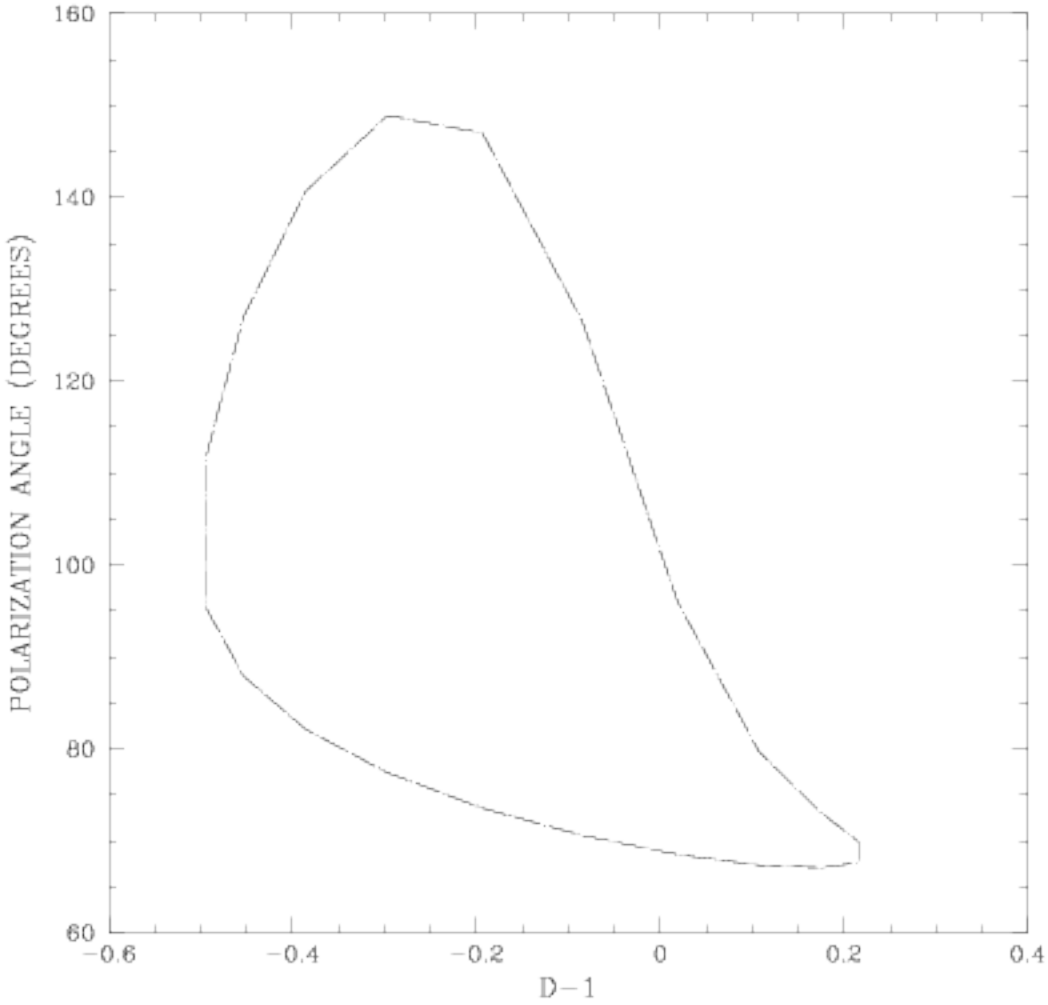

Figure 5.11: Calculation of figure 3 from (Chen and Eardley 1991) using our code. The parameters for this plot are $\theta_o = 60°$, $a = 0$, and $r = 6r_g$. The horizontal axis is $g - 1$ in our notation, and the vertical axis is the polarization angle measured from the β axis. The plane of polarization starts out in the plane of the disk. Our results are indistinguishable from those in Chen and Eardley (1991)

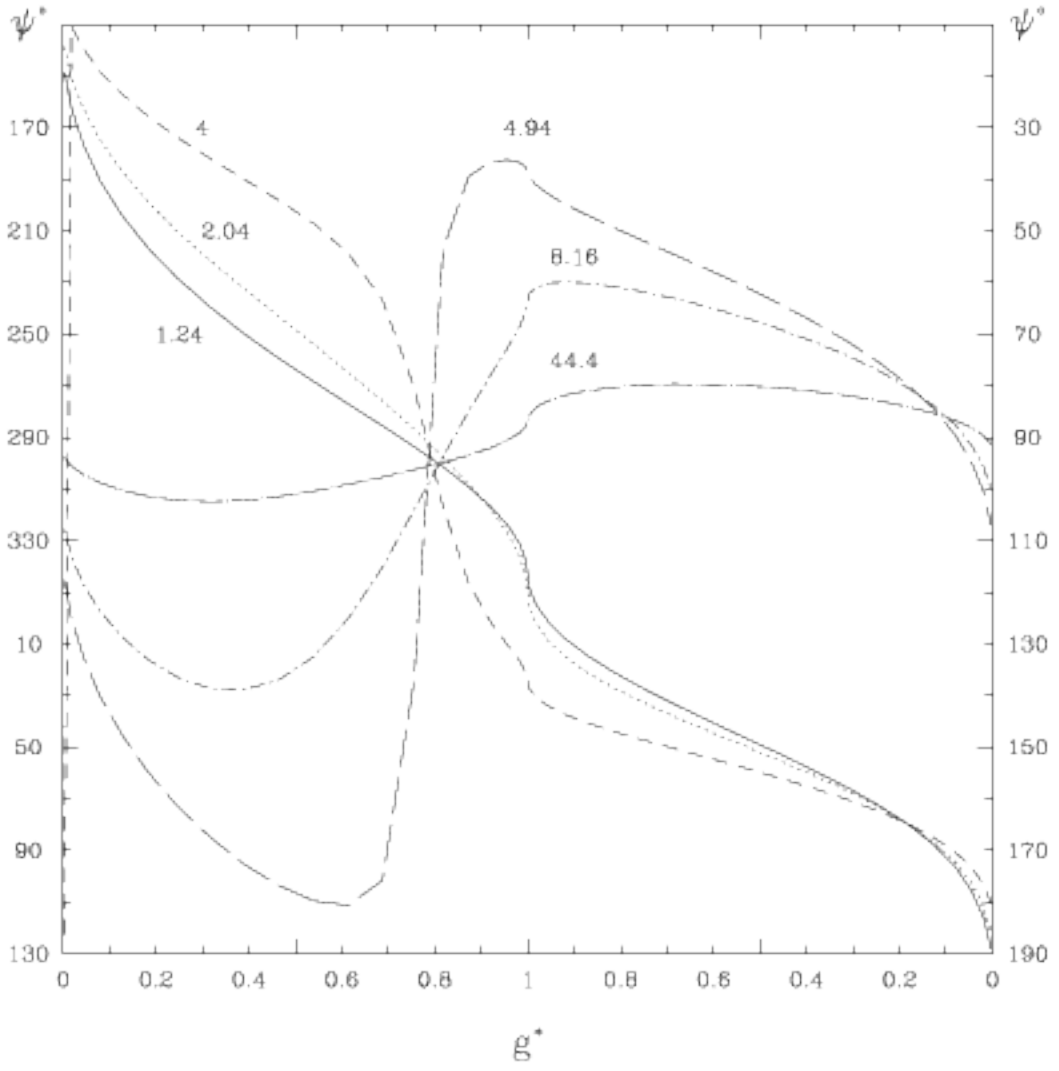

Figure 5.12: Calculation of figure 3 from (Connors, Piran, and Stark 1980). The parameters are $\theta_o = 41.4°$, $a = 0.998$. The curves in the figure are labeled by their radii in terms of r_g. ψ is measured from the β axis. Our results are indistinguishable from Connors et al. (1980) figure 3.